

## RESEARCH LETTER

10.1002/2017GL074903

## Key Points:

- Juno will provide high-accuracy measurements of both the gravity and the magnetic fields of Jupiter
- We propose a new method for using both measurements to estimate the flow structure below the cloud-level
- Two regions are found: an upper region where the flow affects the gravity field and a lower region where it affects the magnetic field

## Supporting Information:

- Supporting Information S1

## Correspondence to:

E. Galanti,  
eli.galanti@weizmann.ac.il

## Citation:

Galanti, E., H. Cao, and Y. Kaspi (2017), Constraining Jupiter's internal flows using Juno magnetic and gravity measurements, *Geophys. Res. Lett.*, *44*, 8173–8181, doi:10.1002/2017GL074903.




Received 12 APR 2017

Accepted 30 JUL 2017

Accepted article online 3 AUG 2017

Published online 26 AUG 2017

## Constraining Jupiter's internal flows using Juno magnetic and gravity measurements

E. Galanti<sup>1</sup> , H. Cao<sup>2</sup> , and Y. Kaspi<sup>1</sup> 

<sup>1</sup>Department of Earth and Planetary Sciences, Weizmann Institute of Science, Rehovot, Israel, <sup>2</sup>Division of Geological and Planetary Sciences, California Institute of Technology, Pasadena, California, USA

**Abstract** Deciphering the flow below the cloud-level of Jupiter remains a critical milestone in understanding Jupiter's internal structure and dynamics. The expected high-precision Juno measurements of both the gravity field and the magnetic field might help to reach this goal. Here we propose a method that combines both fields to constrain the depth-dependent flow field inside Jupiter. This method is based on a mean-field electrodynamic balance that relates the flow field to the anomalous magnetic field, and geostrophic balance that relates the flow field to the anomalous gravity field. We find that the flow field has two distinct regions of influence: an upper region in which the flow affects mostly the gravity field and a lower region in which the flow affects mostly the magnetic field. An optimization procedure allows to reach a unified flow structure that is consistent with both the gravity and the magnetic fields.

### 1. Introduction

The winds engulfing Jupiter, manifested in the planet's cloud motion, have been studied and analyzed extensively, resulting in a robust spatial picture of their amplitude and direction [Porco *et al.*, 2003; Choi and Showman, 2011]. However, their behavior below the clouds remains largely unknown. Aside from the single direct measurement of the flow below the clouds by the Galileo probe at a specific location near 6°N [Atkinson *et al.*, 1996], there is very little knowledge about the nature of the flow underneath the observable clouds. Starting in August 2016, the Juno spacecraft began measuring a range of physical parameters including the planetary magnetic and gravity fields while orbiting Jupiter at unprecedented proximity [Bolton *et al.*, 2017]. These measurements, once calibrated and analyzed, will provide unprecedented latitude- and longitude-dependent high-precision maps of both fields, which can be used to construct the depth-dependent flow field of Jupiter.

Several studies examined the connection between the flow within Jupiter and the spatial variations in the planetary gravity field. It was shown that the gravity field measurements could be used to infer the internal structure of the flow below its cloud-level [Hubbard, 1999; Kaspi *et al.*, 2010; Kaspi, 2013], with the underlying assumption of geostrophic balance for low Rossby number flows [Pedlosky, 1987]. This leads to thermal wind balance between the flow and the density fields. These density perturbations will manifest in the latitudinal variations of the gravity field. Subsequent studies examined in more detail the flow-density relation [Zhang *et al.*, 2015; Kaspi *et al.*, 2016; Cao and Stevenson, 2017b; Galanti *et al.*, 2017a].

The flow field within Jupiter has the potential of being further constrained by the planetary magnetic field. The strong magnetic field of Jupiter (around 6 Gauss at the surface) could affect the flow field at depth with modestly high electrical conductivity [Liu *et al.*, 2008; Heimpel and Gómez Pérez, 2011; Gastine *et al.*, 2014; Jones, 2014; Connerney *et al.*, 2017]. Using models based on electrical conductivity estimates and comparing the wind-induced Ohmic dissipation to the observed planetary luminosity, Liu *et al.* [2008] estimated that the measured magnetic field strength limits the maximum depth to which fast zonal flows can penetrate to 0.96 of the radius for Jupiter. Glatzmaier [2008] argued that this depth could be an overestimate due to the possible geometrical alignment between the deep zonal flow and magnetic fields. Other studies found that the flow itself could alter the magnetic field in the semiconducting region [Heimpel and Gómez Pérez, 2011; Gastine *et al.*, 2014; Cao and Stevenson, 2017a]. This modification could be detectable by the Juno magnetic field experiments [Cao and Stevenson, 2017a].

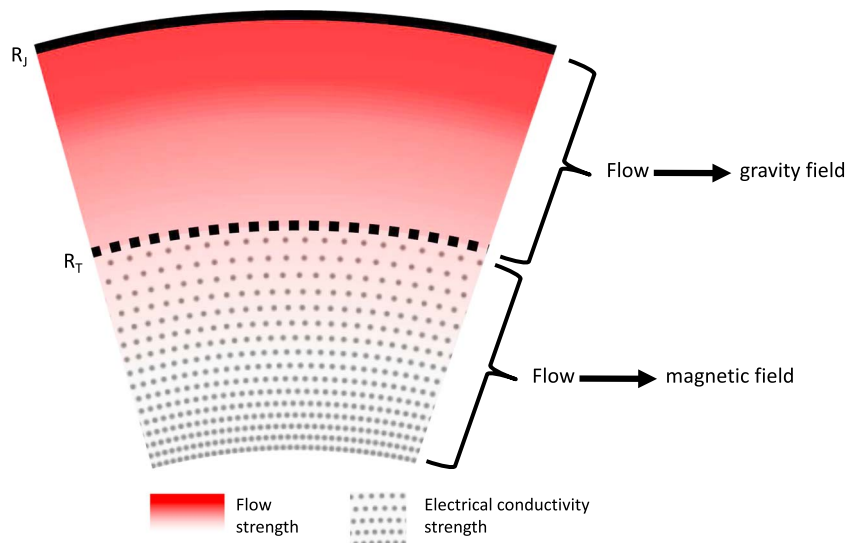


**Figure 1.** A conceptual look at the two regions affecting the anomalous gravity and magnetic fields. An upper region between the planet surface  $R_J$  and a transition level  $R_T$ , and a lower region below  $R_T$ . Shown are the strength of the flow (from red to white), where solid red denotes the wind at the cloud-level and white denotes a few order of magnitude smaller values, and the strength of the electrical conductivity (gray dots where dense dots represent high electrical conductivity and sparse dots represents low electrical conductivity).

The two distinctly different dynamical regimes inside Jupiter are conceptually presented in Figure 1. Starting from the planet’s upper surface,  $R_J$ , the measured cloud-level wind is assumed to decay toward the interior (fading red color). This flow pattern, when translated to density perturbations via the thermal wind balance [e.g., Kaspi et al., 2010; Galanti and Kaspi, 2016], has an integrated signature on the gravity field. This effect has a strong depth dependency—a density perturbation with the same magnitude will have a larger effect on the gravity field when located closer to the planet’s surface. Alongside this dynamical effect, there exists the interaction between the flow and the magnetic field. Below a transition depth  $R_T$ , the electrical conductivity (grained area) increases to a large enough value so the flow can generate sensible magnetic perturbations [Cao and Stevenson, 2017a]. This results in an anomalous latitude-dependent magnetic field. Thus, the interior flow has two distinct regions of influence: an upper region (between  $R_J$  and  $R_T$ ) in which the flow affects mostly the gravity field and a lower region (below  $R_T$ ) in which the flow affects mostly the magnetic field. To date, there has been no study that couples the flow-magnetic balance and the flow-gravity balance to constrain the flow field in a unified approach. In this study we address this issue and propose a new method for using the expected Juno measurements of both the gravity and magnetic fields in order to constrain the depth-dependent flow field inside Jupiter.

The manuscript is organized as follows: in section 2 we describe the mean-field electrodynamics (MFED) and thermal wind (TW) models and present the experimental setup. In section 3 we discuss the optimized solutions of the flow in the MFED and TW models, and the results of the optimization when a unified decay function is used. We conclude in section 4.

## 2. Methodology

### 2.1. The Mean-Field Electrodynamic Balance

The model used here is based on the study of Cao and Stevenson [2017a]. The steady state balance between the anomalous magnetic field and the flow is

$$\eta_E \left( \nabla^2 - \frac{1}{s^2} \right) B + \frac{1}{r} \frac{d\eta_E}{dr} \frac{\partial(rB)}{\partial r} = -\mathbf{B}_0 \cdot \nabla U, \tag{1}$$

$$\eta_E \left( \nabla^2 - \frac{1}{s^2} \right) A = -\alpha B, \tag{2}$$

where  $A(r, \theta)$  and  $B(r, \theta)$  compose the anomalous magnetic field  $\mathbf{B} = \nabla \times (A\hat{e}_\phi) + B\hat{e}_\phi$ ,  $\eta_E(r)$  is the effective magnetic diffusivity,  $s = r \sin \theta$  is the distance from the axis of rotation,  $\mathbf{B}_0(r, \theta)$  is the background planetary

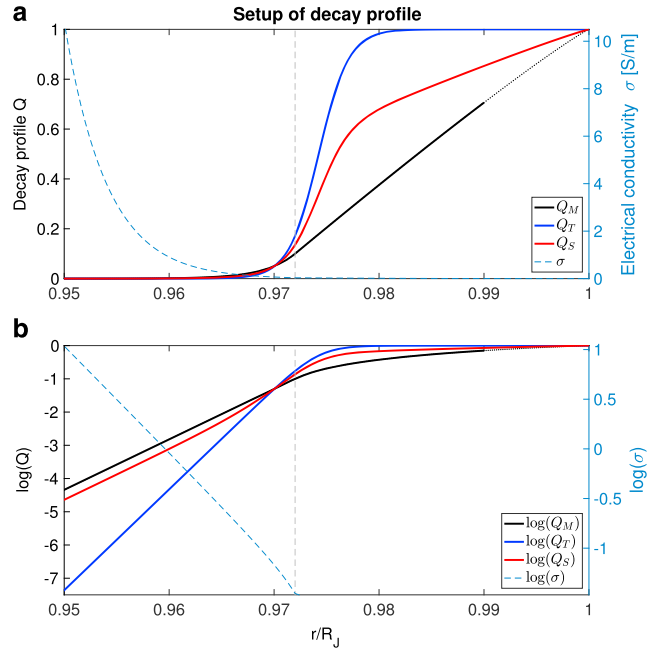


**Figure 2.** (a) A MFED decay factor  $Q_M$  (black), a TW decay factor  $Q_T$  (blue), and their average  $Q_S$  (red). The solid black line is the radial range in which the MFED model is solved. Also shown is the electrical conductivity  $\sigma$  in the MFED model, which controls the strength of the interaction between the flow field and the magnetic field. (b) The log of the fields shown in Figure 2a, illustrating the exponential nature (straight lines) of the decay in the inner layer in both functions.

magnetic field,  $\alpha(r, \theta)$  is the dynamo  $\alpha$ -effect, and  $U(r, \theta)$  is the zonal flow. The magnetic diffusivity is inversely proportional to the electrical conductivity  $\sigma(r)$ . The background magnetic field  $\mathbf{B}_0 = B_0^r \hat{e}_r + B_0^\theta \hat{e}_\theta$  is defined as a dipole field with  $B_0^r(\theta, r) = 2g_0^0 r^{-3} \cos(\theta)$ , and  $B_0^\theta(\theta, r) = g_0^0 r^{-3} \sin(\theta)$ , where  $g_0^0$  is the dipole Gauss coefficient. Note that including quadrupole and octupole moments in the background magnetic field ( $\mathbf{B}_0$ ) has negligible effect on the results in this study (see supporting information).

The flow  $U_M(r, \theta)$  is defined as

$$U_M(r, \theta) = U_{\text{surf}}(s)Q_M(r), \quad (3)$$

$$Q_M(r) = [1 + (f_M - 1)] \left( \frac{r - R_J}{R_T - R_J} \right)^D, \quad r > R_T \quad (4)$$

$$Q_M(r) = f_M \exp\left(\frac{r - R_T}{H_M}\right), \quad r \leq R_T \quad (5)$$

where  $U_{\text{surf}}(s)$  is the measured cloud-level wind projected toward the planet interior parallel to the spin axis (hence its dependence on  $s$ ),  $R_J$  is the planetary radius,  $R_T$  is the transition depth set to  $0.972R_J$ ,  $f_M$  is the ratio between the flow strength at the transition depth and the flow at the cloud-level,  $H_M$  is the decay scale height in the inner layer, and  $D = \frac{(R_J - R_T)f_M}{(1 - f_M)H_M}$  ensures the smoothness of wind across the transition depth. The measured wind  $U_{\text{surf}}(s)$  used here is based on Porco et al. [2003] [e.g., see Galanti and Kaspi, 2016, Figure 1a].

This functional form of the flow's radial decay allows two distinctly different behaviors in the two layers. In the outer layer (equation (4)), the decay function represents a nonmagnetic dynamical effect such as the baroclinic thermal wind effect [Kaspi et al., 2009], with the free parameter  $H_M$  allowing a wide range of flow structures. In the inner layer (equation (5)), the exponential decay function is assumed to be a result of the increased electrical conductivity  $\sigma$  (shown in Figure 2, dashed blue lines). The strength of the electrical conductivity controls the effect of the flow  $U$  on the anomalous magnetic field  $\mathbf{B}$ .

There are two physical reasons for choosing the transition depth to be at  $0.972 R_J$ . First, the depth at which the Lorentz force could balance the observed surface Reynolds stress is around  $0.972 R_J$ . Second, projecting the observed equatorial superrotation along the spin axis toward the deep interior of Jupiter, its deepest point

is at  $0.972 R_J$ . Furthermore, the possibility of a dynamo layer close to  $0.972 R_J$  can be safely ruled out given our understanding of the electrical conductivity of hydrogen inside Jupiter [French *et al.*, 2012].

### 2.1.1. Definition of the MFED Optimization

Juno will measure the poloidal component of the magnetic field  $\mathbf{B}^{\text{Juno}} = \nabla \times (A \hat{e}_\phi)$  at the location of the spacecraft. These measurements can then be projected to a radial location inside the planet in which the electrical conductivity is negligible, using potential field continuation. Given the very small electric conductivity above the transition radius  $R_T$ , it is natural to choose  $R_T$  as the depth of comparison. Therefore, the “measurements” to be used in our model are the downward continuation of both  $B_r^{\text{Juno}}$  and  $B_\theta^{\text{Juno}}$  to the depth  $R_T$ ,

$$\begin{aligned} B_r^{\text{obs}} &= B_r^{\text{Juno}}(r = R_T), \\ B_\theta^{\text{obs}} &= B_\theta^{\text{Juno}}(r = R_T). \end{aligned} \quad (6)$$

Our goal is to find the flow structure that will result in an anomalous magnetic field that best matches the measured one. Therefore, a scalar measure (a cost function) [see Galanti and Kaspi, 2016, 2017] for the difference between the measured and the model magnetic fields is to be defined. We set it as the difference between the measurements and the model solution at  $R_T$ , integrated over latitude

$$L = \frac{1}{\pi} \int_{\theta=0}^{\pi} \left[ W_r^M(\theta) (B_r^{\text{obs}} - B_r^{\text{mod}})^2 + W_\theta^M(\theta) (B_\theta^{\text{obs}} - B_\theta^{\text{mod}})^2 \right] d\theta, \quad (7)$$

where  $B_r^{\text{mod}}$  and  $B_\theta^{\text{mod}}$  are the latitudinal-dependent model solutions, and  $W_r^M(\theta)$ ,  $W_\theta^M(\theta)$  are the weights reflecting the uncertainties in the measurements. A gross estimate of the measurements uncertainty due to instruments limitations is 0.01% of the field strength (J. Connerney, private communication, 2016). Given that the measured background dipole field of Jupiter is about  $4 \times 10^5$  nT, the measurements error in the model is  $B_{\text{err}} = 40$  nT. The weights in the cost function are then

$$W_r^M, W_\theta^M \equiv \frac{1}{(B_{\text{err}})^2}. \quad (8)$$

Two parameters control the flow structure in the MFED model, the scale depth of the flow in the inner layer  $H_M$  and the relative strength of the wind at the transition depth  $f_M$ . Searching for the values of these two parameters (that will result in a magnetic field that best matches the measurements) is an optimization problem that can be solved with various techniques. Here we follow the methodology used recently for optimization of the TW model [Galanti and Kaspi, 2016, 2017; Galanti *et al.*, 2017b], in which a solution is searched for iteratively, within the range of  $10 < H_M < 5000$  km and  $0.025 < f_M < 1$ .

### 2.2. The Thermal Wind Balance

Similar to the MFED model, the flow field used in the thermal wind model is based on cloud-level wind, projected into the interior on cylinders parallel to the axis of rotation, and is assumed to decay in the radial direction. In the TW model, the decay profile used in earlier studies [e.g., Galanti and Kaspi, 2016, 2017] was based on an exponential function. This choice might be replaced with any other function that assures a decay of the flow in the radial direction. Here we use a hyperbolic tangent function

$$U_T(r, \theta) = U_{\text{surf}}(s) Q_T(r), \quad (9)$$

$$Q_T(r) = \frac{\tanh\left(-\frac{R_J - H_T - r}{\Delta H_T}\right) + 1}{\tanh\left(\frac{H_T}{\Delta H_T}\right) + 1}, \quad (10)$$

where  $H_T$  is the decay depth and  $\Delta H_T$  is the width of the decay. Note that the hyperbolic function is normalized by its value at the surface of the planet to assure that the surface flow has the value of the measured cloud-level wind. We choose this function in order to allow a better compatibility with the function used in the MFED model (see more details in section 2.3).

Since the planet is rapidly rotating, and we are considering large-scale flows with small Rossby number, the flow is assumed to be geostrophic and in thermal wind balance [e.g., Kaspi *et al.*, 2009, 2010]. Given that only the zonal mean flow in the azimuthal direction is considered, the balance is

$$2\Omega \frac{\partial}{\partial z} (\bar{\rho} U) = g_0 \frac{\partial}{\partial \theta} \rho', \quad (11)$$

where  $\Omega$  is the planetary rotation rate,  $\tilde{\rho}(r)$  is the background density field,  $g_0(r)$  is the mean gravity acceleration in the radial direction, and  $\rho'(r, \theta)$  is the density anomaly associated with the flow field. The equation is solved similarly to the method used in *Galanti and Kaspi* [2017] and *Galanti et al.* [2017b]. The gravity moments (to be compared with the measurements) are then integrated from the density field

$$\Delta J_n^{\text{mod}} = -\frac{2\pi}{MR_J^n} \int_0^{R_J} r^{n+2} dr \int_{\mu=-1}^1 P_n(\mu) \rho'(r, \mu) d\mu, \quad (12)$$

where  $\Delta J_n^{\text{mod}}$ ,  $n = 2, \dots, N$  are the coefficients of the gravity moments,  $M$  is the planet mass,  $P_n$  is the Legendre polynomials, and  $\mu = \cos(\theta)$ .

While the measured gravity field will be in terms of the gravity moments, here we show the results in terms of the actual latitude-dependent gravity anomalies in the radial direction

$$\Delta g_r^{\text{mod}}(\theta) = -\frac{GM}{R_J^2} \sum_n (n+1) P_n(\cos \theta) \Delta J_n^{\text{mod}}, \quad (13)$$

where  $G$  is the gravitational constant [*Kaspi et al.*, 2010]. Note that the gravity field in the real space is completely equivalent to the gravity field in the moment space.

### 2.2.1. Definition of the TW Optimization

The Juno measurements to be used to optimize the TW model are the gravity moments [*Finocchiaro and less*, 2010] from which the static body moments are subtracted

$$\Delta J_n^{\text{obs}} = J_n^{\text{obs}} - J_n^{\text{solid}}, \quad (14)$$

where  $J_n^{\text{obs}}$  are the measured gravity moments, and  $J_n^{\text{solid}}$  are the static body solutions to be taken from a model solution [e.g., *Wahl et al.*, 2017]. Note that for this analysis we will examine the measured gravity as function of latitude  $\Delta g_r^{\text{obs}}(\theta)$  calculated similarly to the model solution (equation (13)).

The cost function, measuring the fit of the model solution to the measurements, can be written in matrix notation as

$$L = (\Delta J^{\text{obs}} - \Delta J^{\text{mod}})^T W_T (\Delta J^{\text{obs}} - \Delta J^{\text{mod}}), \quad (15)$$

where  $(\Delta J^{\text{obs}} - \Delta J^{\text{mod}})$  is a vector of the differences between the measurements and the model solution, and  $W_T$  is a weight matrix to be derived from the covariance matrix of the measurements [*Finocchiaro and less*, 2010; *Galanti et al.*, 2017b]. The parameters to be optimized are the decay depth  $H_T$  and the width of the decay  $\Delta H_T$ , both of which determine the shape of the decay function (equation (9)). The range of the parameters allowed during the optimization is between 100 and 5000 km for both parameters.

### 2.3. Setup of the Simulated Flow Field

Until the Juno measurements become available, we can simulate a flow structure that mimics a possible realistic scenario and use the MFED and TW models to search for the best fit solutions (see details on methodology in *Galanti and Kaspi* [2016, 2017] and *Galanti et al.* [2017b]). In both the MFED and TW models, the cloud-level wind is extended inward as a function of the distance from the axis of rotation based on angular momentum considerations, and the wind velocity decays in the radial direction toward the center of the planet (equations (4), (5), and (9), respectively). The difference between the two models is in the specifics of the radial decay profile. Since the functions are very different from each other, the decay profile to be used for the simulation of the measurements should be such that neither of the two models will be able to fit it perfectly.

In Figure 2 we show examples of decay functions for the MFED model (black line), the TW model (blue line), and the average between the two models (red line). Figure 2b illustrates the exponential nature of the decay in the inner region in both functions. The decay functions were chosen such that at the depth of the transition to the semiconducting region  $R_T$  the MFED function has a value of 0.1 and the TW a value of 0.2. The parameters for the MFED functions are  $H_M = 200$  km and  $f_M = 0.1$ , and for the TW function  $H_T = 1800$  km and  $\Delta H_T = 200$  km. These specific profiles are chosen so that their average is different from the separate profile. We will therefore use the averaged profile ( $Q_5$ , red line) to set the simulated flow; thus, neither model alone can reconstruct the flow field well. Based on this flow structure, the “measured” anomalous magnetic field  $B_r^{\text{obs}}$ ,  $B_\theta^{\text{obs}}$  and the anomalous gravity field  $\delta g_r^{\text{obs}}$  are calculated and shown in Figures 3a and 3b, respectively (red lines).

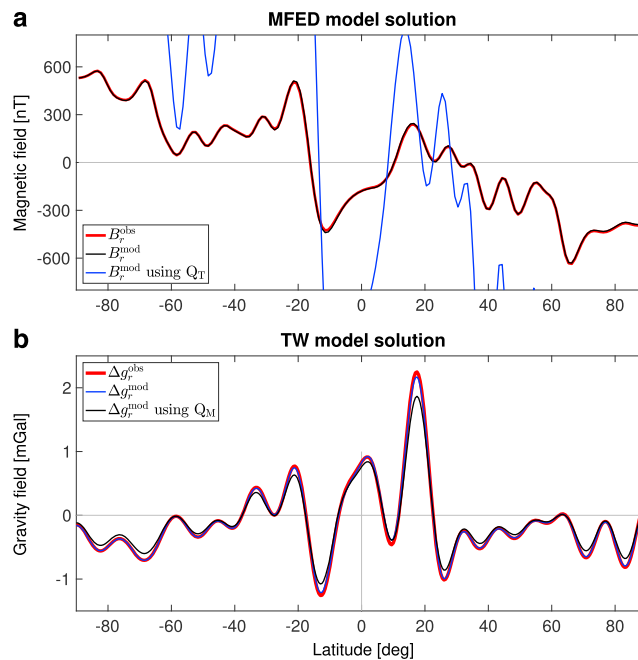


**Figure 3.** (a) The simulated magnetic field (red) and the model optimized solutions (black). (b) The simulated gravity field (red) and the TW model optimized solution (red). Also shown are solutions when the decay profile is taken from the other model solution (blue lines).

### 3. Results

Here we present the results from the optimization of the two models separately, as well as an experiment in which the results from the MFED optimization are used to better constrain the TW model. Note that in all cases, due to the small number of parameters to be optimized, the optimization procedure does not depend on the initial guess of the parameters and that a global minimum is always reached.

#### 3.1. Optimizing the MFED Model Using Magnetic Field Measurements Only

Modifying the values of the parameters  $H_M$  and  $f_M$ , an optimal solution is reached such that the model calculated magnetic field fits best the simulated one. A solution is reached with  $H_M = 168$  km and  $f_M = 0.129$ . Figure 3a shows the simulated radial component of the magnetic field (red line) together with the optimized model calculated field (black line). The match between the solutions is excellent, with a difference that is barely distinguishable on a linear scale. This behavior is underlined in the profile of the optimized decay function (Figure 4a, black line), which is in a very good agreement with the simulated one (Figure 4a, red line) in the inner region, below  $R_T$ . On the other hand, there is less agreement in the region between  $R_J$  and  $R_T$ . This implies that the MFED model is very sensitive below  $R_T$  but less so above this depth. This will become more evident when we discuss the case in which the two model solutions are cross evaluated (section 3.3).

#### 3.2. Optimizing the TW Model Using Gravity Field Measurements Only

Next, we optimize the values of the parameters  $H_T$  and  $\delta H_T$  that gives a TW model solution of the gravity field that best fit the simulated one. A solution is reached with  $H_T = 1504$  km  $\delta H_T = 543$  km. Figure 3b shows the simulated anomalous gravity field (red line) together with the optimized model calculated field (blue line). Similar to the case with the MFED model alone, the match between the simulation and the model solution is remarkably good, with only minor differences, for example, around latitudes 17°S and 17°N. This fit is not trivial given that the profile of the optimized decay function (Figure 4a, blue line) is overestimating in the region below  $R_T$ , underestimating in the region between  $R_T$  and around  $r = 0.98 R_J$ , and again overestimating above that depth. However, the good agreement results from the fact that gravity is an integration of the density over depth (equation (12)); therefore, the integrated contributions of the density perturbations are such that their depth-dependent deviations from the simulation are somewhat canceled. This will be better illustrated in section 3.3 where we examine the case in which the two model solutions are cross evaluated.



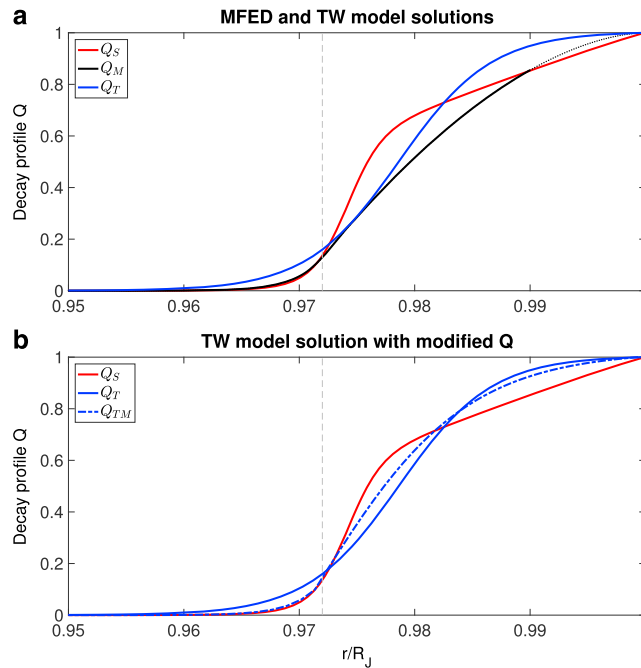


**Figure 4.** (a) The radial decay factor used to simulate the flow (red), the MFED solution (black), and the TW solution (blue). For the MFED solution, the solid black line denotes the radial range in which the magnetic field is solved for. (b) The improved TW solution (dash-dotted blue line) shown together with the simulation (red) and the standard TW solution (solid blue).

### 3.3. Crossing the Decay Function Solutions

It is clear from the previous two experiments that both models can reach a very good fit with the measurements, even though the flow structure they find is not in full agreement with the simulated one. Given that our main goal is to reconstruct the flow structure, it is important to better understand this discrepancy. A simple test for the validity of the decay profiles found by the two models is to switch between the optimized profiles and examine the effect on the calculated magnetic and gravity fields.

First, we use the TW model solution for the decay function  $Q_T$  (Figure 4a, blue line) to calculate the anomalous magnetic field in the MFED model. The resulting field (Figure 3a, blue line) is about an order of magnitude stronger than the simulated one, emphasizing the sensitivity of the MFED model to the strength of the flow below  $R_T$ . The overestimation of the TW solution at that depth, while having very little influence on the gravity field, has a much larger impact on the magnetic field. Next, we use the MFED solution for the decay function  $Q_M$  (Figure 4a, black line) to calculate the gravity field in the TW model. The result (Figure 3b, black line) is not as a good fit to the simulation as was the TW model optimized solution. Overall, the resulting gravity field is weaker than the simulated one, since  $Q_M$  is significantly underestimating the strength of the flow almost everywhere between  $R_T$  and  $R_J$ . The better estimation below  $R_T$  has little effect on the calculated gravity field.

### 3.4. Optimizing the TW Model Using a Unified Decay Function

Given the results of the above experiment, we now examine an estimation of the flow structure combining both models. The MFED model captures very well the decay of the winds below the transition depth  $R_T$ . This solution can be used to constrain further the TW model solution by using a modified decay function that is allowed to vary only above  $R_T$  and is set to have the values of the MFED solution from that depth and inward. For simplicity, we also assume that the depth  $R_T$  is the inflection point of the hyperbolic tangent. The new function to be optimized with the TW model can be approximated as

$$Q_{TM}(r) = \tanh\left(-\frac{R_T - r}{\delta H_T}\right) \left[ \tanh^{-1}\left(-\frac{R_T - R_J}{\delta H_T}\right) - f_M \right] + f_M, \quad R_T < r < R_J, \quad (16)$$

$$Q_{TM}(r) = f_M \exp\left(\frac{r - R_T}{H_M}\right), \quad r \leq R_T. \quad (17)$$

We can now optimize again the TW model, with the width of the hyperbolic tangent  $\delta H_T$  being the only parameter to be optimized. The optimized solution is reached with  $\delta H_T = 870$  km. The optimized profile is shown in Figure 4b (dash-dotted blue line) together with the previous less constrained profile (solid blue line) and the decay profile used for the simulation (red line). In addition to the values below  $R_T$  that are now identical to the MFED model solution, the values above  $R_T$  are now in a much better agreement with the decay function used for the simulation. In the region close to the surface of the planet, the wind decays more, and in the region closer to the transition depth  $R_T$  it decays less. This new profile  $Q_{TM}$  can now be used also in the MFED model with a resulting magnetic field that is in excellent agreement with the simulation.

#### 4. Conclusions

A new coupled method is proposed for combining the gravity and magnetic field measurements from the Juno mission, in order to decipher the flow structure below Jupiter's cloud-level. We do so using a mean-field electrodynamic balance that relates the flow field to the anomalous magnetic field, and geostrophic balance (implying also thermal wind balance) that relates the flow field to the anomalous gravity field. A flow structure that fits neither model perfectly is used to simulate the measurements, therefore posing a nontrivial problem for the optimization of the models.

We find that the decay profile of the flow can be fitted in both models to give a very good match to the simulated measurements, even though the two decay profile solutions differ significantly from one another. The reason for that apparent paradox is that there are two separate regions of influence (Figure 1). An upper region (between  $R_J$  and  $R_T$ ) in which the flow is strong and in which no interaction with the magnetic field exists, and a lower region (below  $R_T$ ) in which the flow is weak but is affecting the magnetic field strongly.

Importantly, placing an effective constraint on the strength of deep zonal flows in the semiconducting region of Jupiter does not require a fit as good as reached in this study. For example, an absence of strongly banded magnetic field in the observations would already impose strong constraints on the amplitude and vertical scale height of zonal flows in the semiconducting region. Furthermore, separating the dynamo-generated magnetic field from the wind-induced magnetic field is not trivial. As pointed out in *Cao and Stevenson [2017a]*, one way to overcome this difficulty would be to perform local inversions of the measured magnetic field in order to extract  $B_r$  at a limited latitudinal band. Since we do not expect the dynamo-generated magnetic field to feature structures at length scales that are similar to the surface zonal wind length scale, such local inversions could help identify small-scale features in  $B_r$  that are correlated with surface winds. Note also that while here we use a simplified  $\alpha$ -effect, a more complex  $\alpha$ -effect with latitudinal dependence, as well as the  $\gamma$ -effect [*Kapyla et al., 2006*], are certainly possible. However, while adding complexity to the expected solutions, including these parameters would not change the method presented in our study.

Crossing the results from the two models, i.e., using the decay profile solution from the TW model to calculate the magnetic field, and using the decay profile solution from the MFED model to calculate the gravity field, shows the discrepancies between the two approaches. The TW profile's overestimation of the flow amplitude at the lower region results in a magnetic field that is an order of magnitude larger than the simulated one, and the MFED profile's underestimation of the flow amplitude in the upper region results in a gravity field that is about 20% weaker than the simulated measurements. One way to overcome the discrepancy, and therefore to utilize both approaches combined, is offered. A new profile is set for the TW model, such that in the lower region the solution from the MFED model is used, and in the upper region a new profile is optimized consistently with the lower region values.

The Juno measurements, to date, have already reformed our understanding of Jupiter's interior from the gravity [*Folkner et al., 2017; Kaspi et al., 2017; Wahl et al., 2017*], microwave [*Li et al., 2017*], and magnetic measurements [*Connerney et al., 2017; Moore et al., 2017*]. This study presents the first unified approach for combining these measurements, taking advantage of the sensitivity of the magnetic and gravity fields to different depth regimes within the planet. As the measurements become more abundant this approach may be beneficial in building an understanding of the 3-D flow within the planet.

#### References

- Atkinson, D. H., J. B. Pollack, and A. Seiff (1996), Galileo doppler measurements of the deep zonal winds at Jupiter, *Science*, 272, 842–843.  
Bolton, S. J., A. Adriani, V. Adumitroaie, J. Anderson, and the Juno Science Team (2017), Jupiter's interior and deep atmosphere: The first close polar pass with the Juno spacecraft, *Science*, 356, 821–825.

#### Acknowledgments

This research has been supported by the Israeli Ministry of Science and the Minerva foundation with funding from the Federal German Ministry of Education and Research. E.G. and Y.K. also acknowledge support from the Helen Kimmel Center for Planetary Science at the Weizmann Institute of Science. Most of the numerical information is provided in the figures produced by solving the equations in the paper. Any additional data may be obtained from E.G. (e-mail: eli.galanti@weizmann.ac.il).



- Cao, H., and D. Stevenson (2017a), Zonal flow magnetic field interaction in the semi-conducting region of giant planets, *Icarus*, *296*, 59–72, doi:10.1016/j.icarus.2017.05.015.
- Cao, H., and D. J. Stevenson (2017b), Gravity and zonal flows of giant planets: From the euler equation to the thermal wind equation, *J. Geophys. Res. Planets*, *122*, 686–700, doi:10.1002/2017JE005272.
- Choi, D. S., and A. P. Showman (2011), Power spectral analysis of Jupiter's clouds and kinetic energy from Cassini, *Icarus*, *216*, 597–609.
- Connerney, J. E. P., et al. (2017), Jupiter's magnetosphere and aurorae observed by the Juno spacecraft during its first polar orbits, *Science*, *356*(6340), 826–832.
- Finocchiaro, S., and L. Iess (2010), Numerical simulations of the gravity science experiment of the Juno mission to Jupiter, in *Spaceflight Mechanics*, vol. 136, pp. 1417–1426, Amer. Astro. Soc., San Diego, Calif.
- Folkner, W., et al. (2017), Jupiter gravity field from first two Juno orbits, *Geophys. Res. Lett.*, *44*, 4694–4700, doi:10.1002/2017GL073140.
- French, M., A. Becker, W. Lorenzen, N. Nettelmann, M. Bethkenhagen, J. Wicht, and R. Redmer (2012), Ab initio simulations for material properties along the Jupiter adiabat, *Astrophys. J. Suppl. Ser.*, *202*(1), 5.
- Galanti, E., and Y. Kaspi (2016), An adjoint-based method for the inversion of the Juno and Cassini gravity measurements into wind fields, *Astrophys. J.*, *820*(2), 91.
- Galanti, E., and Y. Kaspi (2017), Decoupling Jupiter's deep and atmospheric flows using the upcoming Juno gravity measurements and a dynamical inverse model, *Icarus*, *286*, 46–55.
- Galanti, E., Y. Kaspi, and E. Tziperman (2017a), A full, self-consistent treatment of thermal wind balance on oblate fluid planets, *J. Fluid Mech.*, *810*, 175–195.
- Galanti, E., D. Durante, S. Finocchiaro, L. Iess, and Y. Kaspi (2017b), Estimating Jupiter gravity field using Juno measurements, trajectory estimation analysis, and a flow model optimization, *Astron. J.*, *154*(1), 2.
- Gastine, T., J. Wicht, L. D. V. Duarte, M. Heimpel, and A. Becker (2014), Explaining Jupiter's magnetic field and equatorial jet dynamics, *Geophys. Res. Lett.*, *41*, 5410–5419, doi:10.1002/2014GL060814.
- Glatzmaier, G. A. (2008), A note on "constraints on deep-seated zonal winds inside Jupiter and Saturn", *Icarus*, *196*, 665–666.
- Heimpel, M., and N. Gómez Pérez (2011), On the relationship between zonal jets and dynamo action in giant planets, *Geophys. Res. Lett.*, *38*, L14201, doi:10.1029/2011GL047562.
- Hubbard, W. B. (1999), Note: Gravitational signature of Jupiter's deep zonal flows, *Icarus*, *137*, 357–359.
- Jones, C. A. (2014), A dynamo model of Jupiter's magnetic field, *Icarus*, *241*, 148–159.
- Kapyla, P. J., M. J. Korpi, M. Ossendrijver, and M. Stix (2006), Magnetoconvection and dynamo coefficients—III.  $\alpha$ -effect and magnetic pumping in the rapid rotation regime, *Astron. Astrophys.*, *455*(2), 401–412.
- Kaspi, Y. (2013), Inferring the depth of the zonal jets on Jupiter and Saturn from odd gravity harmonics, *Geophys. Res. Lett.*, *40*, 676–680, doi:10.1029/2012GL053873.
- Kaspi, Y., G. R. Flierl, and A. P. Showman (2009), The deep wind structure of the giant planets: Results from an anelastic general circulation model, *Icarus*, *202*, 525–542.
- Kaspi, Y., W. B. Hubbard, A. P. Showman, and G. R. Flierl (2010), Gravitational signature of Jupiter's internal dynamics, *Geophys. Res. Lett.*, *37*, L01204, doi:10.1029/2009GL041385.
- Kaspi, Y., J. E. Davighi, E. Galanti, and W. B. Hubbard (2016), The gravitational signature of internal flows in giant planets: Comparing the thermal wind approach with barotropic potential-surface methods, *Icarus*, *276*, 170–181.
- Kaspi, Y., E. Galanti, R. Helled, Y. Miguel, W. B. Hubbard, B. Militzer, S. Wahl, S. Levin, J. Connerney, and S. Bolton (2017), The effect of differential rotation on Jupiter's low-degree even gravity moments, *Geophys. Res. Lett.*, *44*, 5960–5968, doi:10.1002/2017GL073629.
- Li, C., et al. (2017), The distribution of ammonia on Jupiter from a preliminary inversion of Juno microwave radiometer data, *Geophys. Res. Lett.*, *44*, 5317–5325, doi:10.1002/2017GL073159.
- Liu, J., P. M. Goldreich, and D. J. Stevenson (2008), Constraints on deep-seated zonal winds inside Jupiter and Saturn, *Icarus*, *196*, 653–664.
- Moore, K. M., J. Bloxham, J. E. P. Connerney, J. L. Jørgensen, and J. M. G. Merayo (2017), The analysis of initial Juno magnetometer data using a sparse magnetic field representation, *Geophys. Res. Lett.*, *44*, 4687–4693, doi:10.1002/2017GL073133.
- Pedlosky, J. (1987), *Geophysical Fluid Dynamics*, Springer, New York.
- Porco, C. C., et al. (2003), Cassini imaging of Jupiter's atmosphere, satellites and rings, *Science*, *299*, 1541–1547.
- Wahl, S., et al. (2017), Comparing Jupiter interior structure models to Juno gravity measurements and the role of an expanded core, *Geophys. Res. Lett.*, *44*, 4649–4659, doi:10.1002/2017GL073160.
- Zhang, K., D. Kong, and G. Schubert (2015), Thermal-gravitational wind equation for the wind-induced gravitational signature of giant gaseous planets: Mathematical derivation, numerical method, and illustrative solutions, *Astrophys. J.*, *806*(2), 270.